Springer

KSME

Journal of Mechanical Science and Technology 33 (1) (2019) 157~172
www.springerlink.com/content/1738-494x(Print)/1976-3824(Online)
DOI 10.1007/s12206-018-1216-3

The FERgram: A rolling bearing compound fault diagnosis based on maximal overlap discrete wavelet packet transform and fault energy ratio †

Shuting Wan and Bo Peng*

Department of Mechanical Engineering, North China Electric Power University, Baoding 071003, China

(Manuscript Received June 11, 2018; Revised August 18, 2018; Accepted August 26, 2018)

Abstract

Compound fault features of the rolling bearing are difficult to separate and extract. To address this problem, the present paper proposed a diagnosis algorithm, namely FERgram, on the base of maximal overlap discrete wavelet packet transform (MODWPT) and fault energy ratio (FER). First, a group of frequency band signals are gained after MODWPT processing the initial vibration signal. Second, FER is chosen as the evaluation index, and then the FER values of each frequency band signal are calculated and used to generate FERgram. The frequency band signal with the maximum FER value containing plentiful fault information is chosen for envelope analysis. Finally, the fault type is determined by contrasting the prominent frequency component of the envelope spectrum with the fault feature frequency. The feasibility and superiority of the FERgram method are verified by four signals and four comparison methods. The results show that the FERgram method can effectively extract and accurately diagnose the compound fault of rolling bearing.

Keywords: Rolling bearing; Diagnosis; Compound fault; MODWPT; FER

1. Introduction

Rolling bearing is commonly used in rotating machinery, and its working status influences the safe and reliable operation of equipment [1-3]. At present, most rolling bearing fault diagnosis methods only pay attention to the single fault. However, the compound fault often occurs due to the bad working conditions in actual operation. Under the compound fault of rolling bearing, different fault characteristics intermingle and interfere with each other [4]. Consequently, the effective diagnosis of bearing fault became increasingly complicated.

Blind source separation (BSS) [5] can separate the single fault characteristic from the compound fault signal of rolling bearing. However, due to the limitation of installation position and working conditions, it is not realistic to place multiple sensors in mechanical devices to collect multi-channel signals, and thus BSS cannot be widely used. In order to address the underdetermined problem of BSS, Wang et al. [6] presented a method that integrated ensemble empirical mode decomposition with independent component analysis (EEMD-ICA), which broke through the application limitation of blind signal processing technology under underdetermined condition. As a result, the compound fault characteristics of rolling bearings under different rotational speeds were successfully separated. Cui et al. [7] proposed a method that the single channel signal is decomposed into a group of narrow band signals by null-space pursuit algorithm, and those narrow band components are combined with the original signal into a new set of observation signals. Consequently, the underdetermined problem is overcame, and the single fault source signal is finally obtained by the blind source separation. Ming et al. [8] first performed orthogonal wavelet transform that the single channel signal is decomposed into various sub-band signal components, and then the feature information of the inner and outer ring contained in the sub-band component is strengthened by the spectrum autocorrelation method. Therefore, this method successfully separated the compound fault characteristics. Li [9] adopted morphological component analysis algorithm, where the single channel compound fault signal is segmented into various sparse signals, and the separation of different fault features is successfully realized. However, constructing an overcomplete representation dictionary is complex in this method.

Compared with above methods, envelope demodulation is a fast and simple method, where the pivotal step is to precisely identify the frequency band that contains plentiful fault information. For purpose of selecting the frequency band adaptively, Antoni creatively proposed spectral kurtosis theory [10, 11] and fast kurtogram method [12], both of which attracted many scholars' attention for their effectiveness and superiority in bearing fault diagnosis. After that, many improvements are proposed to enhance the diagnostic ability of the original Fast

*Corresponding author. Tel.: +86 15933962296, Fax.: +86 312 7525026
E-mail address: ncepupengbo@163.com
† Recommended by Associate Editor Sungsoo Na

Kurtogram method. The improved methods are mainly divided into two categories, one is to change the frequency band decomposition process [13-16], the other is to alter the evaluating indicator to identify the frequency band that containing the most fault information [17-23]. The above methods are all aimed at the single fault, and the results for diagnosing the compound fault are not good.

According to the spectral kurtosis theory, the present paper put forward a compound fault diagnosis method of the rolling bearing established on MODWPT and FER, namely FERgram. Distinct from the fast kurtogram method, the FERgram method used MODWPT rather than finite impulse response filters or the short time Fourier transform to generate more precise filters. The FER calculated based on the Teager energy spectrum is chosen as a new evaluation index substituting the kurtosis index. The present method can effectively separate and accurately identify the compound fault of rolling bearing, thanks to the excellent frequency band decomposition performance of MODWPT and the frequency tracking characteristic of the FER.

2. Proposed method

2.1 Maximal overlap discrete wavelet packet transform

Wavelet packet transform (WPT) possess favorable time-frequency localization characteristic, and is used as an efficient filter to segment the initial signal into a group of frequency band signals. However, there are two shortcomings of WPT that cannot be ignored. One is the signals extracted from the wavelet packet nodes are not ranked from low to high in frequency. The other is that the number of signal data halves at each decomposition level. MODWPT algorithm can overcome the above two shortcomings, and the detailed information can be seen in the Refs. [24]. In addition, the decomposition performance of MODWPT is superior to that of WPT.

The principle of discrete wavelet transform (DWT) is as follows: $\{X_t, t = 0, ..., N\text{-}1\}$ is a real valued time series, N is an integer multiple of 2. $\{g_l, l = 0, 1, ..., L\text{-}1\}$ and $\{h_l, l = 0, 1, ..., L\text{-}1\}$ are low pass and high pass filters respectively, L is the length of the filter. g_l and h_l meet the following equations.

$$\begin{aligned} &\sum_{l=0}^{L-1} g_l^{\,2} = 1, \sum_{l=0}^{L-1} g_l g_{l+2n} = \sum_{l=-\infty}^{l=+\infty} g_l g_{l+2n} = 0 \\ &h_l = (-1)^l g_{L-l-1}, g_l = (-1)^{l+1} h_{L-l-1} . \end{aligned} \tag{1}$$

$\{V_{j\text{-}1,t}, t = 0, \dots, N_{j\text{-}1}\text{-}1\}$ is the jth level scale transformation coefficients, where $N_j = N/2j$ and $V_{0,t} = X_t$. Based on Mallat algorithm, the jth level scaling transform coefficients $V_{j,t}$ and wavelet transform coefficients $W_{j,t}^{'}$ of DWT are calculated respectively.

$$\begin{aligned} V_{j,t} &= \sum_{l=0}^{l-1} g_l V_{j-1,(2t+1-l)\bmod N_j-1} \qquad \left(t = 0, ..., N_j - 1\right) \\ W_{j,t} &= \sum_{l=0}^{l-1} h_l V_{j-1,(2t+1-l)\bmod N_j-1} \qquad \left(t = 0, ..., N_j - 1\right) \end{aligned} \tag{2}$$

where mod represents remainder after division.

MODWT is a modified version of DWT, which is a highly redundant non-orthogonal wavelet transform and does not require sample size N. MODWT redefine the filters.

$$\overline{g}_l = g_l / \sqrt{2}, \overline{h}_l = h_l / \sqrt{2} . \tag{3}$$

$\overline{g}$ and $\overline{h}$ meet the following equations.

$$\begin{aligned} &\sum_{l=0}^{L-1} \overline{g}_l^{\,2} = 1, \sum_{l=0}^{L-1} \overline{g}_l \overline{g}_{l+2n} = \sum_{l=-\infty}^{l=+\infty} \overline{g}_l \overline{g}_{l+2n} = 0 \\ &\overline{h}_l = (-1)^l \overline{g}_{L-l-1}, \overline{g}_l = (-1)^{l+1} \overline{h}_{L-l-1} . \end{aligned} \tag{4}$$

MODWT contains the weighted average of all observation starting points in the sequence, which can suppress the deviation caused by cyclic displacement. In order to avoid the problem that the number of signal data halves at each decomposition level, MODWPT rebuilds suitable filters at different jth level by inserting $2^{j\text{-}1}$ zeros in $\{g_l\}$ and $\{h_l\}$.

$$\begin{aligned} &\overline{g}_0, 0, ..., 0, \overline{g}_1, 0, ..., 0, \ldots \overline{g}_{L-2}, 0, ..., 0, \overline{g}_{L-1} \\ &\overline{h}_0, 0, ..., 0, \overline{h}_1, 0, ..., 0, \ldots \overline{h}_{L-2}, 0, ..., 0, \overline{h}_{L-1} . \end{aligned} \tag{5}$$

Based on Mallat algorithm, the jth level scaling transform coefficients $V_{j,t}^{'}$ and wavelet transform coefficients $W_{j,t}^{'}$ of MODWT are as follows

$$\begin{aligned} V_{j,t}^{'} &= \sum_{l=0}^{l-1} \overline{g}_l V_{j-1,(2t+1-l)\bmod N_t-1} \qquad \left(t = 0, ..., N_j - 1\right) \\ W_{j,t}^{'} &= \sum_{l=0}^{l-1} \overline{h}_l V_{j-1,(2t+1-l)\bmod N_t-1} \qquad \left(t = 0, ..., N_j - 1\right) . \end{aligned} \tag{6}$$

The transformation coefficient of MODWT has good performances, such as translation invariance, fixed time resolution under each decomposition level and phase not distorted, et al. MODWPT is put forward on the basis of MODWT, keeps the good performance of MODWT and can decompose the high frequency part of the signal very well. MODWPT coefficient $W_{j,n}$ can be calculated as:

$$\begin{aligned} &W_{j,n,t} = \sum_{l=0}^{l-1} r_{n,t} W_{j-1,[n/2],(t-2^{j-1})\bmod N} \qquad \left(t = 0, ..., N_j - 1\right) \\ &n \bmod 4 = 0 \ \ or\ 3,\ r_{n,t} = \left\{\overline{g}_l\right\} \\ &n \bmod 4 = 1 \ \ or\ 2,\ r_{n,t} = \left\{\overline{h}_l\right\} \end{aligned} \tag{7}$$

where j is the transform levels, n is frequency band number under each transform level. Fig. 1 shows MODWPT decomposition tree, where the transform levels is 3 and Fs represents the sampling frequency. The real part of each $W_{j,n}$ represents the sub-band component of the original signal in different frequency range.

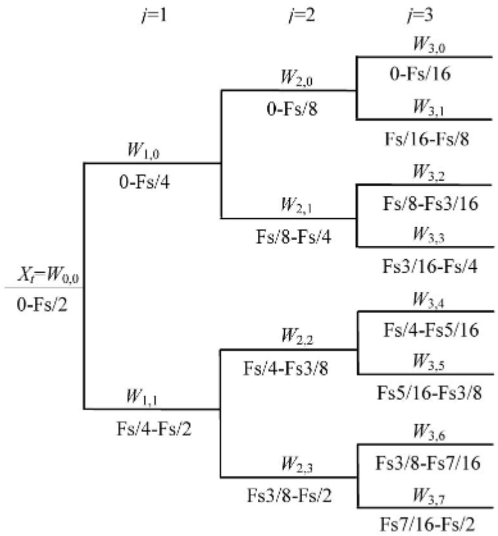

Fig. 1. The decomposition process of MODWPT.

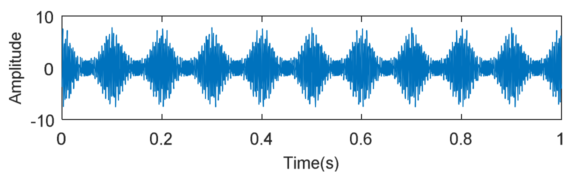

Fig. 2. Waveform of $x(t)$ in time domain.

A three-component AM-FM signal is used to prove the above conclusion and is defined as:

$$\begin{cases} x(t) = x_1(t) + x_2(t) + x_3(t) \\ x_1(t) = 1.5\cos(20\pi t)\sin(1200\pi t + \cos(20\pi t)) \\ x_2(t) = (3 + 3\cos(20\pi t))\sin(700\pi t + 5\cos(10\pi t)) \\ x_3(t) = \cos(10\pi t)\sin(400\pi t + 0.8\cos(20\pi t)) \end{cases} \quad (8)$$

where sampling point N = 3000, sampling frequency Fs = 3000 Hz, simulation time t = 1 s.

Fig. 2 shows the AM-FM signal waveform. The transform level of MODWPT and WPT is 4. The time-frequency diagram obtained by MODWPT and WPT is presented in Figs. 3(a) and (b), respectively. The waveform in Fig. 3(a) is clearer than that in Fig. 3(b), indicating that MODWPT has better decomposition accuracy than WPT. Correspondingly, the vibration signal of rolling bearing in compound fault condition, which is also a multi-component AM-FM signal, can be decomposed more efficiently by MODWPT.

2.2 Fault energy ratio

Fault energy ratio (FER) was first reported in Ref. [25], which is calculated based on the envelope spectrum and can distinguish and evaluate the periodic impact caused by different bearing fault type. Under strong noise interference, Teager energy spectrum can extract the frequency characteristics of weak impact better than envelope spectrum does [26]. Built on

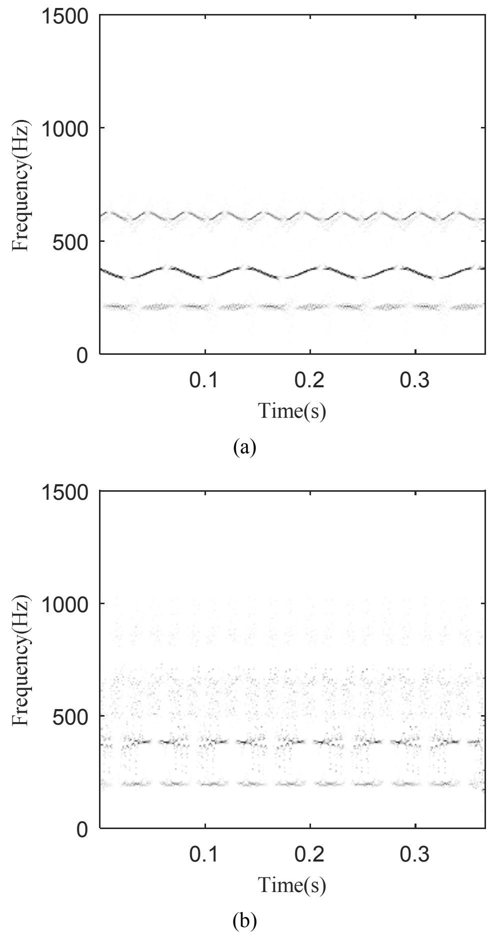

Fig. 3. Time-frequency diagram: (a) MODWPT; (b)WPT.

this superiority, the Teager energy spectrum instead of envelope spectrum is used to calculate the FER value in the present paper. The FER values of different fault type can be obtained by the following steps:

Step 1: According to the definition of Teager energy operator, the instantaneous energy signal is obtained after the following operation, which is displayed in Eq. (9).

$$\psi\left[x(t)\right] = \left[x'(t)\right]^2 - x(t)x''(t) \quad (9)$$

where $x'(t)$ and $x''(t)$ is the first and two order derivatives of the signal $x(t)$, respectively.

Step 2: Teager energy spectrum is obtained by FFT transformation of the instantaneous energy signal.

Step 3: The FER value of different fault type is calculated by the follow equation:

$$FER(f') = \frac{\text{FE}}{\text{SE}} = \frac{\sum_{n=1}^{5} A^2(nf')}{\sum A^2(f)} \quad (f' = f_i, f_o, f_e \, or \, f_c) \quad (10)$$

where FE and SE denotes fault energy and signal total energy respectively. $A(f)$ is the amplitude of each frequency in Teager energy spectrum. $A(nf')$ is the amplitude of the fault feature frequency and its frequency doubling in Teager energy spectrum. f' represents the feature frequency of the different fault type. f_i represents the fault frequency of the inner ring (IRFF), f_o represents the fault frequency of the outer ring (ORFF), f_e represents the fault frequency of the rolling element (REFF), f_c represents the fault frequency of the cage (CFF). The feature frequency of different fault type is calculated by the mathematical formulas listed below [27].

$$f_i = \frac{Z}{2}(1+\frac{d}{D}\cos\alpha)\frac{N}{60} \qquad f_o = \frac{Z}{2}(1-\frac{d}{D}\cos\alpha)\frac{N}{60}$$
$$f_e = \frac{D}{2d}(1-\left(\frac{d}{D}\cos\alpha\right)^2) \qquad f_c = \frac{1}{2}(1-\frac{d}{D}\cos\alpha)\frac{N}{60} \tag{11}$$

where d and D represents the diameter of the balls and the pitch respectively; α represents the contact angle between the ball and the raceway; Z represents the number of rolling element; N represent the rotating speed.

2.3 Diagnosis method based on MODWPT and FER

Thanks to the excellent frequency band decomposition performance of MODWPT and the frequency tracking characteristic of FER, the present paper put forward a compound fault diagnosis method of the rolling bearing established on MODWPT and FER, namely FERgram. Fig. 4 describes the diagnosis process.

Step 1: A group of distinct frequency band signals are gained after MODWPT algorithm processing the initial vibration signal.

Step 2: The FER values of different frequency band signals are calculated and then presented in the FERgram, where the lateral and vertical axis represents the frequency and the decomposition level of MODWPT respectively. Fig. 5 shows the schematic diagram of FERgram. Each node of FERgram represents the narrowband signal obtained by MODWPT decomposition, and these narrowband signals are in the different frequency bands. For example, node (2, 2) represents the narrowband signal with a bandwidth of Fs/8 Hz and a central frequency of 3Fs/16 Hz. The color depth of FERgram represents the FER values of each frequency band signal. A higher FER value shows that the signal contains more fault information.

Step 3: The frequency band signal with the maximum FER value among different FERgram is selected for the envelope analysis.

Step 4: The fault type is identified by contrasting the frequency components corresponding to the prominent spectral lines in the envelope spectrum with the fault feature frequency.

3. Validations for the proposed method

In the following content, a simulation signal, a synthetic signal and two experimental signals are processed by five methods: the EEMD-ICA method [6], the spectral kurtosis improved by WPT (WPT-SK) [13], the enhanced Kurtogram (E-Kurtogram) method [14], the TEERgram method [23], and the FERgram method.

Table 1. Simulation parameters.

	Outer ring fault	Inner ring fault
Fault amplitude	1	1
Fault frequency	50 Hz	130 Hz
Natural frequency	1500 Hz	2800 Hz
Shaft frequency	20 Hz	
Sampling frequency	8192 Hz	
Sampling points	8192	

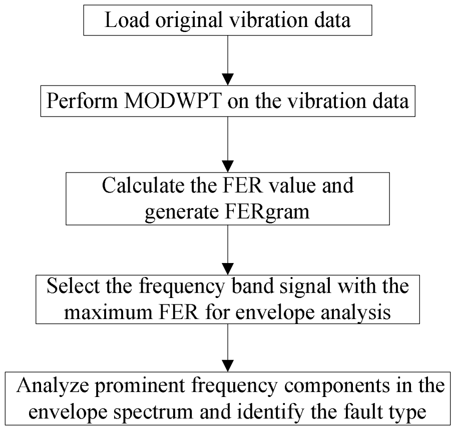

Fig. 4. The diagnosis process of the proposed method.

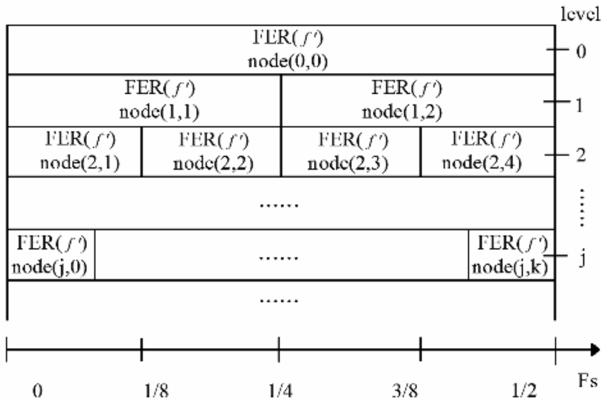

Fig. 5. The schematic diagram of FERgram.

3.1 Simulation signal analysis

The vibration signal of the rolling bearing compound fault can be simulated by two periodic impulse signal overlaying gauss noise signal [27]. Table 1 is the basic parameters of the simulation signal.

Figs. 6(a)-(d) displays the simulation signal waveform of the outer ring fault, inner ring fault, gauss noise (SNR =

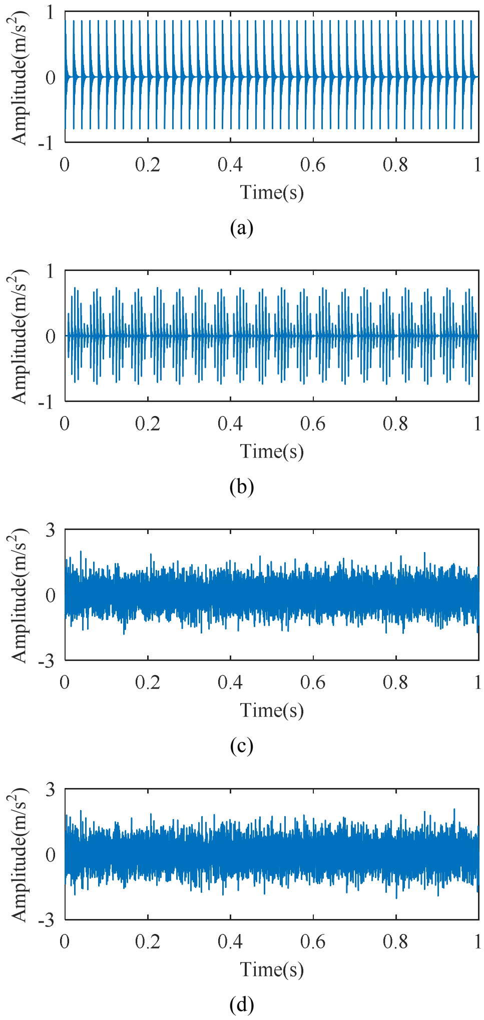

Fig. 6. Simulation signal waveform: (a) Outer ring fault; (b) inner ring fault; (c) gauss noise; (d) compound fault mixed by (a)-(c).

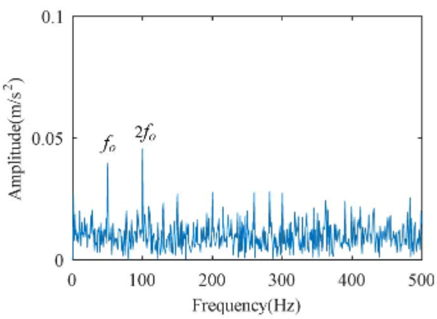

Fig. 7. Envelope spectrum (ES) of Fig. 3(d).

-8 dB) and compound fault, respectively. As shown in Fig. 6(d), the periodic transient impulse characteristics caused by fault are submerged by gauss noise. Fig. 7 displays the envelope spectrum (ES) of the compound fault simulation signal. As seen, the ORFF f_o and its frequency doubling $2f_o$ are identified whereas the IRFF f_i cannot be extracted.

The compound fault simulation signal is processed by EEMD-ICA method. According to the diagnostic process in

Table 2. Correlation coefficient of IMFs.

IMF1	IMF2	IMF3	IMF4	IMF5	IMF6	IMF7
1	0.7771	0.4629	0.3013	0.2293	0.1611	0.1236
IMF8	IMF9	IMF10	IMF11	IMF12	IMF13	IMF14
0.0802	0.0530	0.0310	0.0309	0.0126	0.0044	0.0042

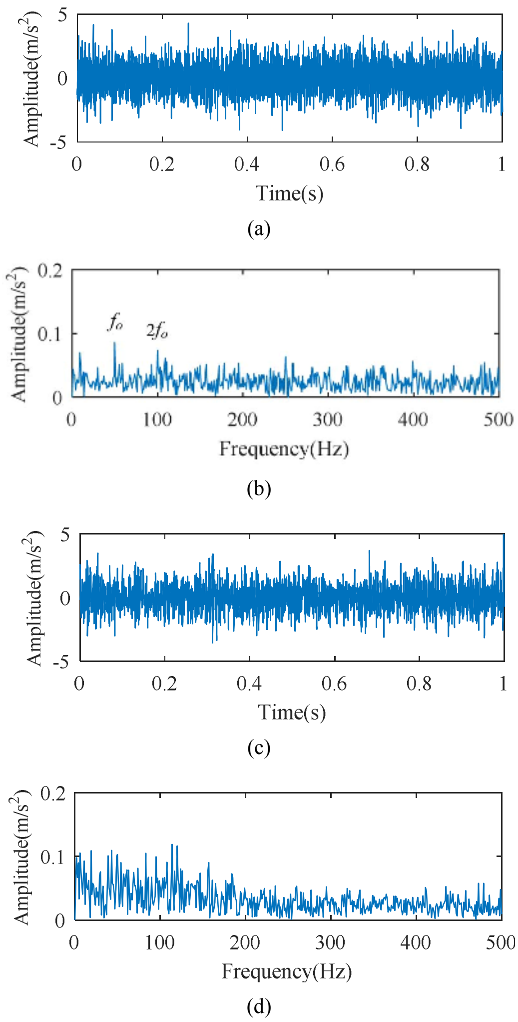

Fig. 8. Diagnosis results of the simulation signal: (a) IC1 signal waveform; (b) ES of IC1; (c) IC2 signal waveform; (d) ES of IC2.

Ref. [6], a series of intrinsic mode functions (IMF) components are firstly obtained after the initial vibration signal processing by EEMD algorithm, and th correlation coefficient of each IMF component of initial signal are calculated and shown in Table 2. The IMF1 - IMF5 component are used as the input parameter for ICA algorithm, for the values of those components are larger. The time waveforms and the ES of the independent component (IC) signals obtained by ICA algorithm are plotted in Fig. 8. As seen, the ORFF f_o and its frequency doubling $2f_o$ are identified whereas the IRFF f_i cannot be extracted.

The compound fault simulation signal is processed by WPT-SK method. According to the diagnostic process in Ref.

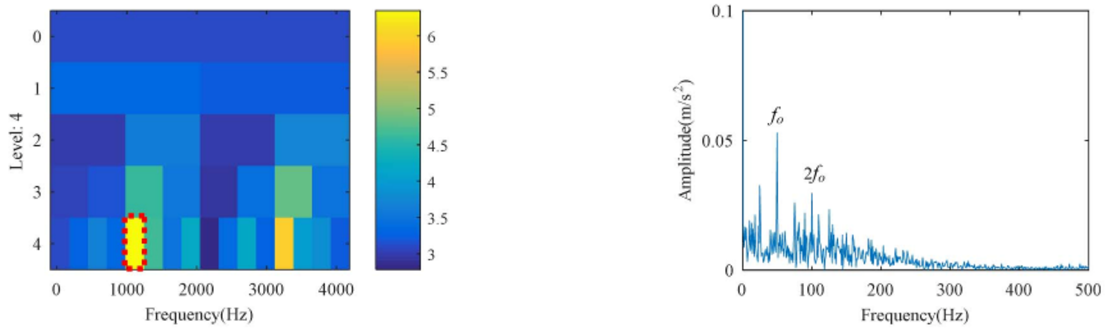

(a) (b)

Fig. 9. Diagnosis results of the simulation signal: (a) Kurtgram; (b) ES of the signal corresponding to node (4, 5) in (a).

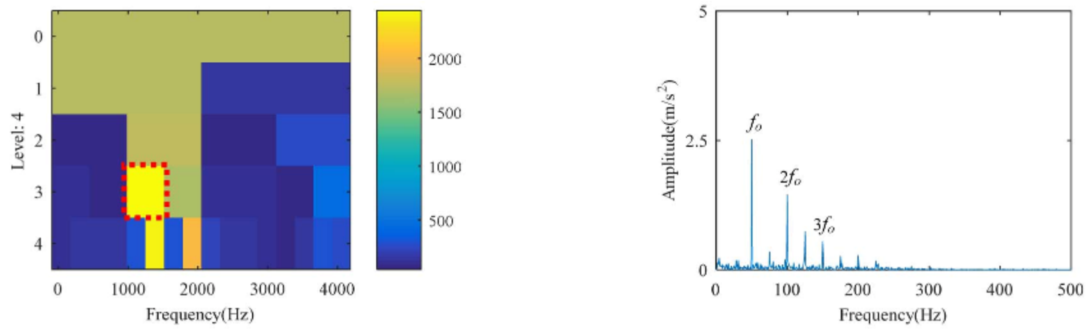

(a) (b)

Fig. 10. Diagnosis results of the simulation signal: (a) E-kurtgram; (b) ES of the signal corresponding to node (3, 3) in (a).

[13], a number of distinct frequency band signals are obtained after the initial vibration signal is processed by WPT algorithm. The kurtosis value of different frequency band signals are calculated and then presented in the kurtgram, where the lateral and vertical axis represents the frequency and the decomposition level of WPT respectively. Each node of kurtgram represents the narrowband signal obtained by WPT decomposition, and these narrowband signals are in the different frequency bands. The signal corresponding to the node with the maximum kurtosis is selected for envelope analysis. Fig. 9(a) presents that node (4, 5) has the maximum kurtosis value. Fig. 9(b) displays the ES of the frequency band signal corresponding to node (4, 5). As seen, the ORFF f_o and its frequency doubling $2f_o$ are identified whereas the IRFF f_i cannot be detected.

The compound fault simulation signal is analyzed by E-Kurtogram method. According to the diagnostic process in Ref. [14], the initial vibration signal is firstly pre-whitened. Then, a group of distinct frequency band signals are obtained after the whitened signal is processed by WPT algorithm. The kurtosis values of the power spectrum of the envelope of different frequency band signals are calculated and then presented in the E-kurtgram, where the lateral and vertical axis represents the frequency and the decomposition level of WPT respectively. Each node of kurtgram represents the narrowband signal obtained by WPT decomposition, and these narrowband signals are in the different frequency bands. The signal corresponding to the node with the maximum kurtosis is selected for envelope analysis. Fig. 10(a) displays that the node (3, 3) has the maximum kurtosis value. Fig. 10(b) illustrates the ES of the frequency band signal corresponding to node (3, 3). As seen, the ORFF f_o and its doubling frequency $2f_o$ - $3f_o$ are identified productively whereas the IRFF f_i cannot be extracted.

The compound fault simulation signal is analyzed by TEERgram method. According to the diagnostic process in Ref. [23], a number of distinct frequency band signals are obtained after the initial vibration signal is processed by WPT algorithm. The teager energy entropy ratio (TEER) value of different frequency band signals are calculated and then presented in the TEERgram, where the lateral and vertical axis represents the frequency and the decomposition level of WPT respectively. Each node of TEERgram represents the narrowband signal obtained by WPT decomposition, and these narrowband signals are in the different frequency bands. The signal corresponding to the node with the maximum TEER is selected for envelope analysis. Fig. 11(a) displays that the node (4, 6) has the maximum TEER value. Fig. 11(b) illustrates the ES of the frequency band signal corresponding to node (4, 6). As seen, the ORFF f_o and its doubling frequency $2f_o$ - $3f_o$ are identified productively whereas the IRFF f_i cannot be extracted.

The compound fault simulation signal is processed by FERgram method. Fig. 12(a) displays the FERgram of inner

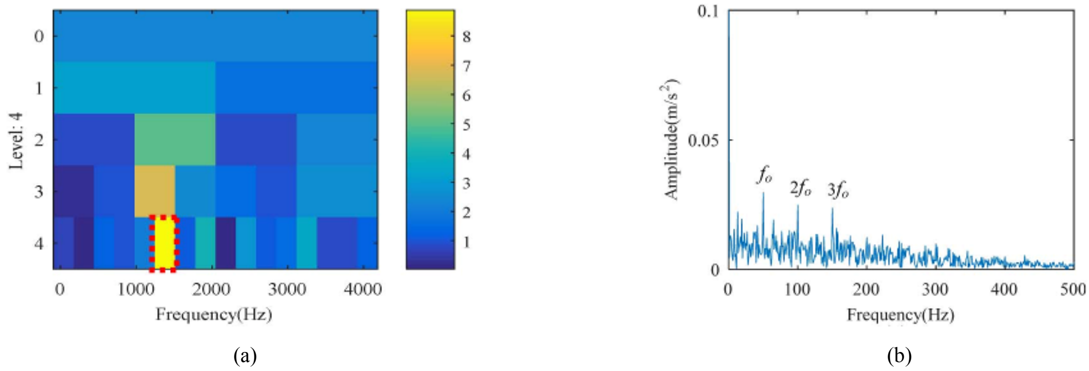

Fig. 11. Diagnosis results of the simulation signal: (a) TEERgram; (b) ES of the signal corresponding to node (4, 6) in (a).

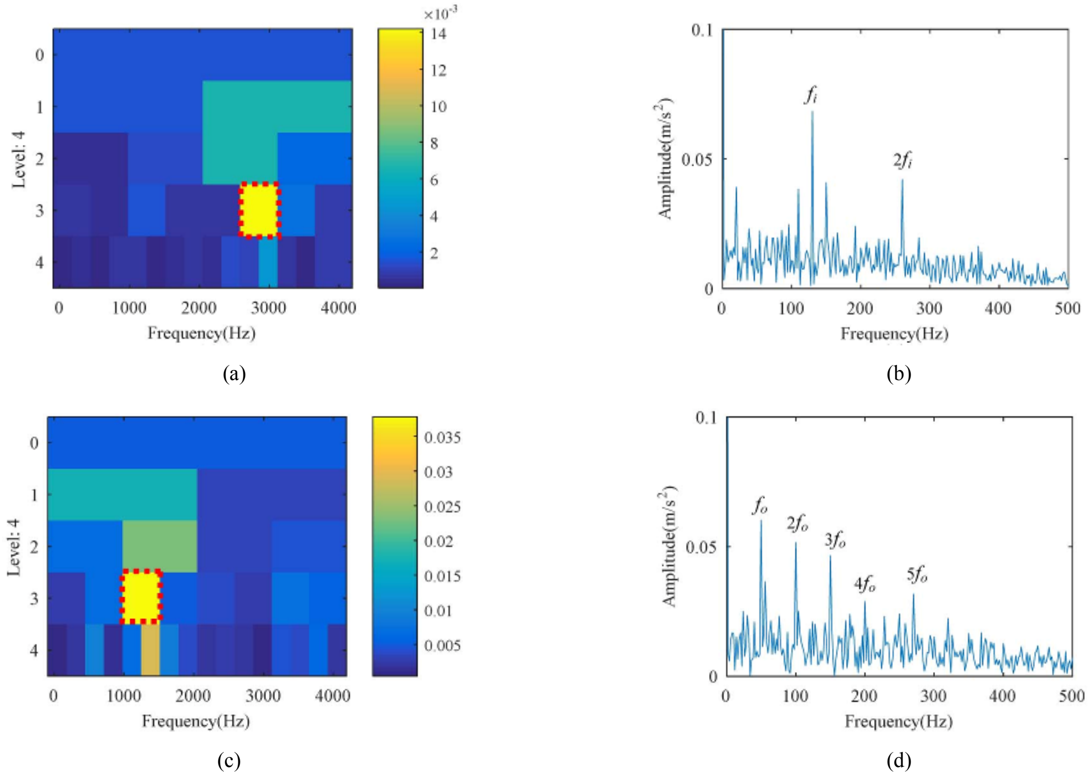

Fig. 12. Diagnosis results of the simulation signal: (a) FERgram of inner ring fault; (b) ES of the signal corresponding to node (3, 6) in (a); (c) FER-gram of outer ring fault; (d) ES of the signal corresponding to node (3, 3) in (c).

ring fault. The maximum FER value is marked by the red rectangle and is at node (3, 6). That is to say, the frequency band signal corresponding to node (3, 6) contained the most inner ring fault information and its ES is diaplayed in Fig. 12(b). As seen, the IRFF f_i and its frequency doubling $2f_i$ are extracted effectively. Fig. 12(c) displays the FERgram of the outer ring fault. As shown, the maximum FER value is marked by the red rectangle and is at node (3, 3). Thus, the frequency band signal corresponding to node (3, 3) is selected, as it contained the most outer ring fault information, and its ES is presented in Fig. 12(d). As seen, the ORFF f_o and its frequency doubling $2f_o$ - $5f_o$ are extracted productively.

In this case, the FERgram method can efficiently separate the fault information and accurately determine that the rolling bearing is under compound fault composed by inner and outer ring defective, while the EEMD-ICA method, WPT-SK method, E-Kurtogram method and TEERgram method cannot realize such functionality.

3.2 Synthetic signal analysis

This paper adopts the synthetic method used in Ref. [28], in which the compound fault signal is synthesized by superposition of two single fault signals. The single bearing vibration signal of Case Western Reserve University is often used by researchers [29]. Fig. 13 shows the test platform. The test

Table 3. SKF6023-2RS bearing parameters.

Outside diameter	Inside diameter	Ball diameter	Pitch diameter	Balls number	Contact angle
40 mm	17 mm	6.7 mm	28.5 mm	8	0°

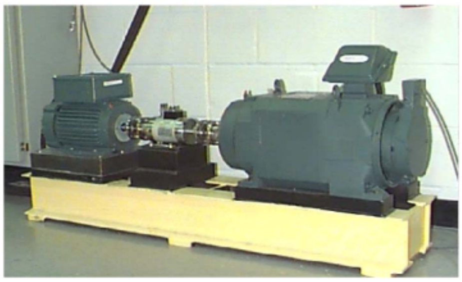

Fig. 13. Test platform of Case Western Reserve University.

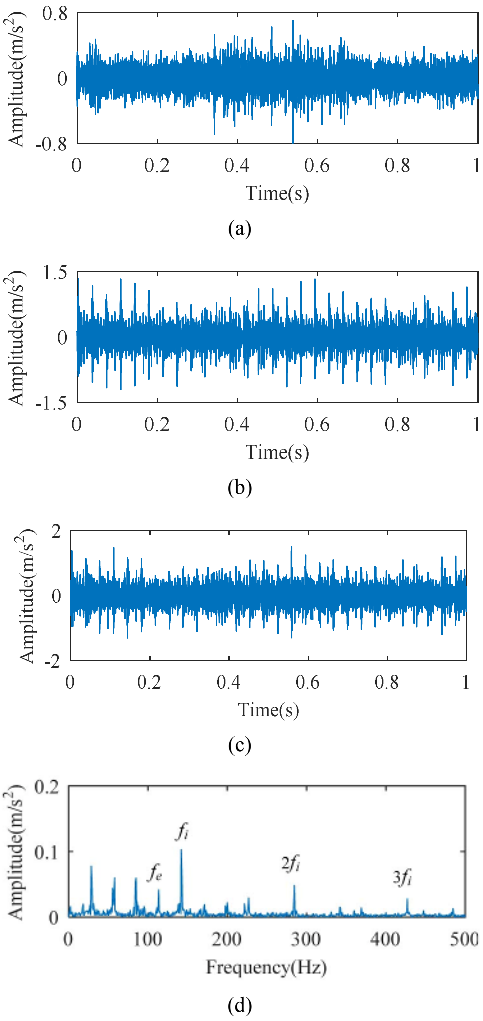

Fig. 14. Signal waveform of case: (a) Inner ring fault; (b) rolling element fault (c) compound fault synthesized by (a) and (b); (d) ES of (c).

bearing is SKF6023-2RS deep grove ball bearing and its basic parameters are listed in Table 3. For simulating the weak fault, a pit (0.07 mm in diameter and 0.011 mm thick) is machined

Table 4. Correlation coefficient of IMFs.

IMF1	IMF2	IMF3	IMF4	IMF5	IMF6	IMF7
1	0.7499	0.6187	0.1992	0.1012	0.0515	0.0231
IMF8	IMF9	IMF10	IMF11	IMF12	IMF13	IMF14
0.0048	0.0046	0.0011	0.0011	0.0009	0.00008	0.0012

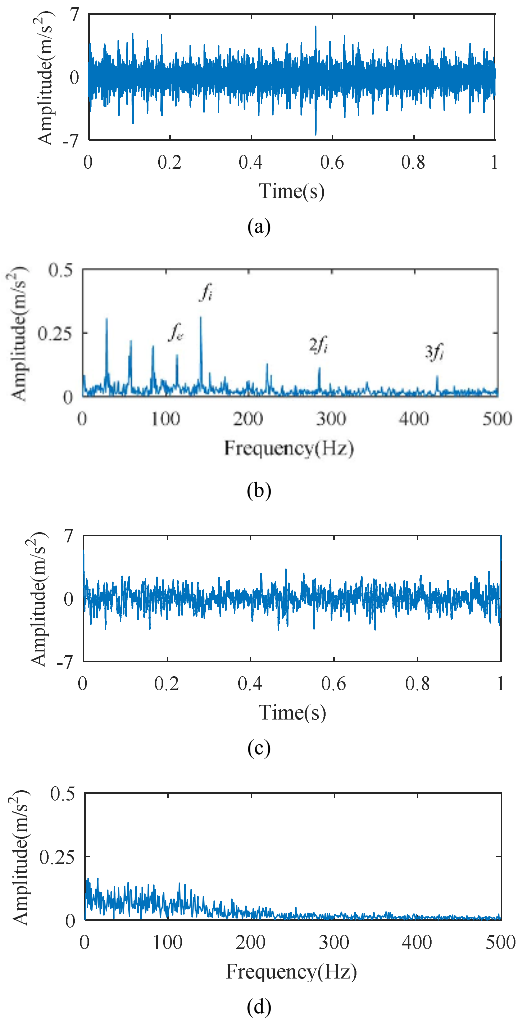

Fig. 15. Diagnosis results of the synthetic signal: (a) IC1 signal waveform; (b) ES of IC1; (c) IC2 signal waveform; (d) ES of IC2.

on the bearing inner ring and rolling element respectively through wire-cutting technology. The shaft rotary speed n = 1478 r/min, the signals are collected by acceleration sensors and the sampling frequency Fs = 12000 Hz. The parameters shown in Table 3 are introduced into the Eq. (11), where the IRFF f_i = 148 Hz, and the REFF f_e = 118 Hz can be obtained.

Figs. 14(a) and (b) show the single signal waveform of inner ring fault and that of rolling element fault, respectively. Figs. 14(c) and (d) display the waveform and ES of the compound fault signal synthesized by the above two single fault signal, respectively. As shown in Fig. 11(d), the IRFF f_i and its frequency doubling $2f_i$ - $3f_i$ are extracted effectively. The REFF f_e can also be identified, but the amplitude of f_e is small-

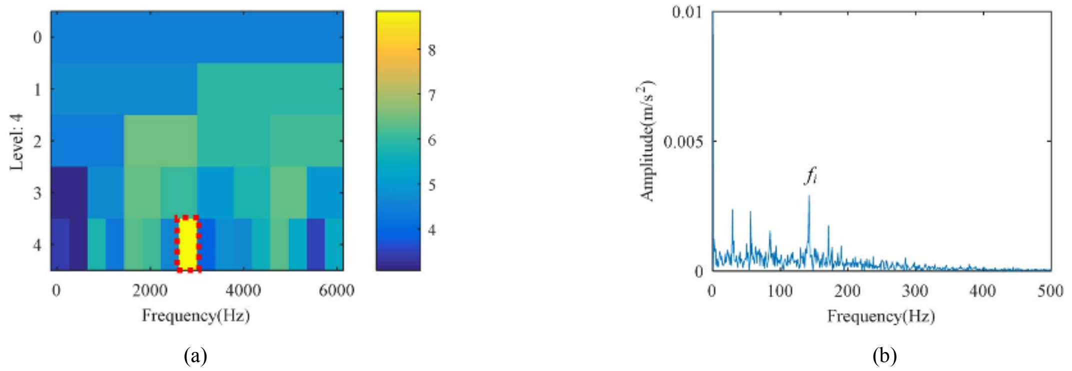

Fig. 16. Diagnosis results of the synthetic signal: (a) Kurtgram; (b) ES of the signal corresponding to node (4, 8) in (a).

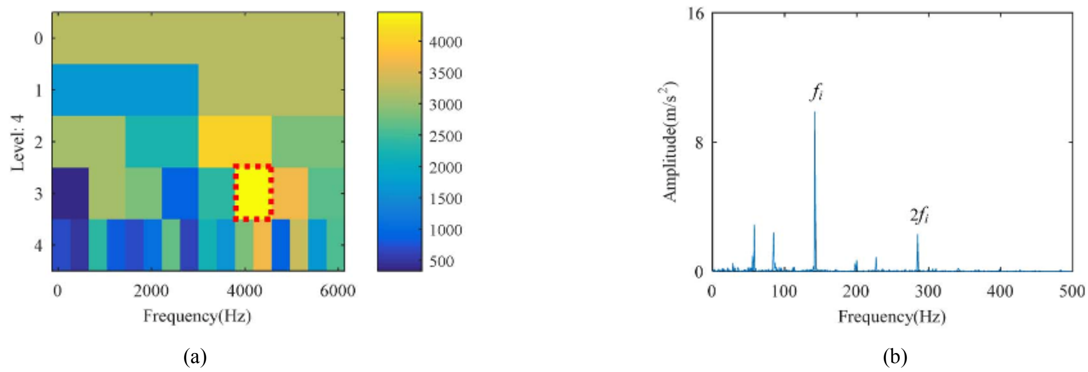

Fig. 17. Diagnosis results of the synthetic signal: (a) E-kurtgram; (b) ES of the signal corresponding to node (3, 6) in (a).

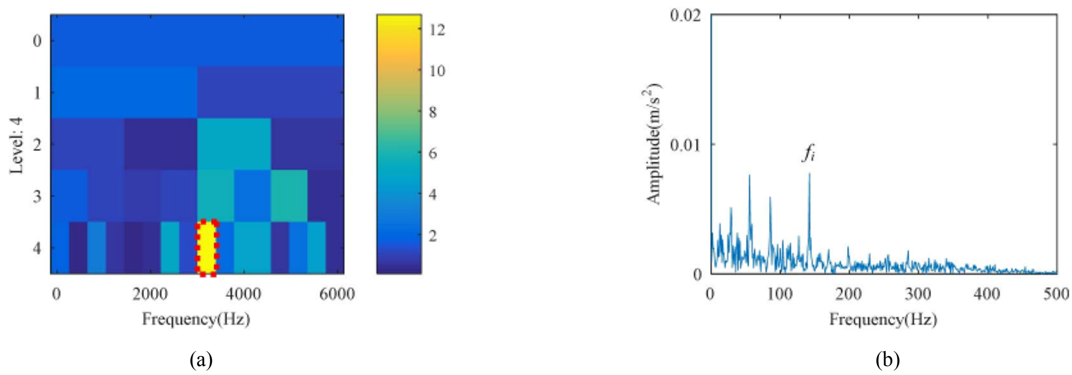

Fig. 18. Diagnosis results of the synthetic signal: (a) TEERgram; (b) ES of the signal corresponding to node (4, 9) in (a).

er than that of f_i and the noise frequency, and thus is usually ignored.

The compound fault synthetic signal is processed by the EEMD-ICA method. Table 4 presents the correlation coefficient of each IMF component of initial signal. The IMF1–IMF6 components are used as the input parameter for ICA algorithm. Fig. 15 displays the diagnosis results. As seen, the REFF f_e can be identified, but is very weak compared with the IRFF f_i and the noise frequency. That is to say, the REFF f_e is usually ignored.

The compound fault synthetic signal is processed by WPT-SK method. Fig. 16(a) displays that the node (4, 8) has the maximum kurtosis value. Fig. 16(b) presents the ES of the frequency band signal corresponding to node (4, 8). As seen, the INFF f_i are identified productively whereas the REFF f_e cannot be extracted.

The compound fault synthetic signal is processed by E-Kurtogram method. Fig. 17(a) displays that the node (3, 6) has the maximum kurtosis value. Fig. 17(b) illustrates the ES of the frequency band signal corresponding to node (3, 6). As seen, the INFF f_i and its doubling frequency $2f_i$ are identified productively whereas the REFF f_e cannot be extracted.

The compound fault synthetic signal is processed by TEERgram method. Fig. 18(a) displays that the node (4, 9) has the maximum kurtosis value. Fig. 18(b) illustrates the envelope spectrum of the frequency band signal correspond-

Table 5. SKF6205 bearing parameters.

Outside diameter	Inside diameter	Ball diameter	Pitch diameter	Balls number	Contact angle
52 mm	25 mm	7.9 mm	39 mm	9	0°

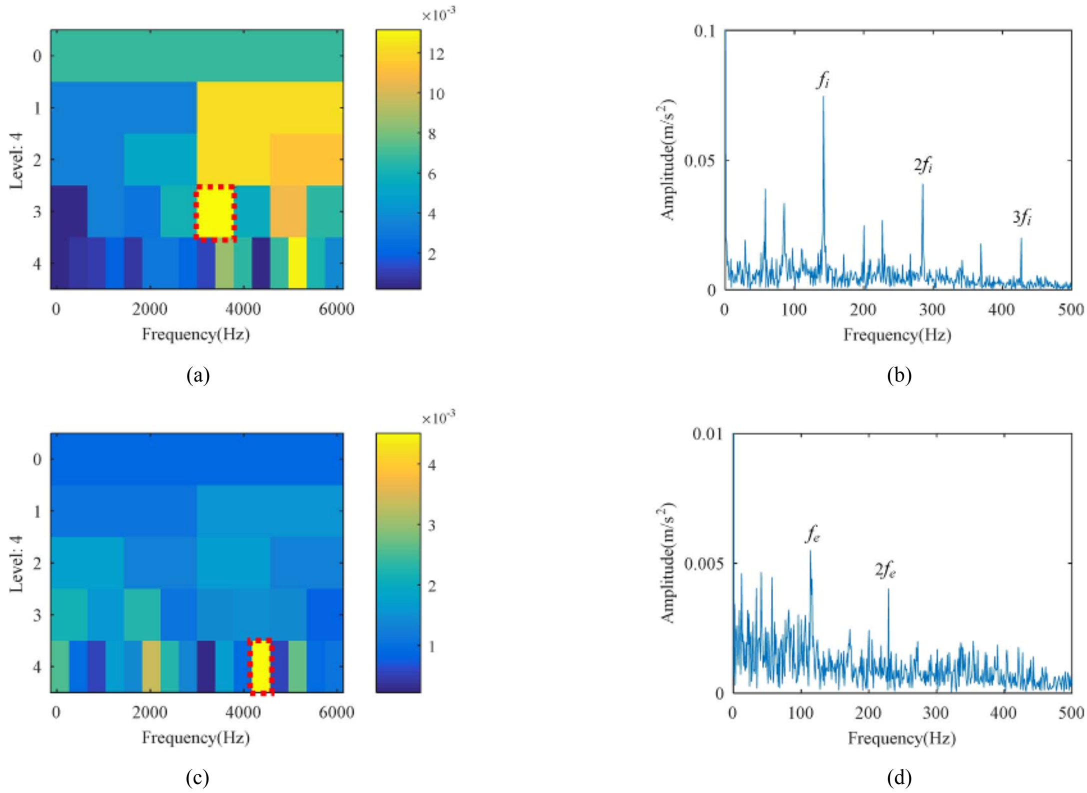

Fig. 19. Diagnosis results of the synthetic signal: (a) FERgram of inner ring fault; (b) ES of the signal corresponding to node (3, 5) in (a); (c) FERgram of rolling element fault; (d) ES of the signal corresponding to node (4, 12) in (c).

ing to node (4, 9). As seen, the INFF f_i is identified productively whereas the REFF f_e cannot be extracted.

The compound fault synthetic signal is processed by FERgram method. Fig. 19(a) displays the FERgram of inner ring fault. As shown, the maximum FER value is marked by the red rectangle and is at node (3, 5). That is to say, the frequency band signal corresponding to node (3, 5) contained the most inner ring fault information and its ES is presented in Fig. 19(b). As seen, the IRFF f_i and its frequency doubling $2f_i$ - $3f_i$ are extracted effectively. Fig. 19(c) displays the FERgram of rolling element fault. As shown, the maximum FER value is marked by the red rectangle and is at node (4, 12). Thus, the frequency band signal corresponding to node (4, 12) is chosen, as it contained the most rolling element fault information, and its ES is displayed in Fig. 19(d). As seen, the REFF f_e and its frequency doubling $2f_e$ are identified productively.

In this case, the FERgram method can efficiently separate the fault information and accurately determine that the rolling bearing is under compound fault composed by inner ring and rolling element defective, while the EEMD-ICA method, WPT-SK method, E-Kurtogram method and TEERgram method cannot realize such functionality.

3.3 Experiment signal 1 analysis

The experimental signal of the rolling bearing under inner and outer ring fault is obtained from QPZZ test platform. Fig. 20(a) displays the QPZZ test platform. The experiment bearing is SKF6205 deep grove ball bearing and its basic parameters are shown in Table 5. Fig. 20(b) displays the groove (1.5 mm in diameter and 0.2 mm thick) is machined on the bearing inner and outer ring respectively through wire-cutting technology. Fig. 20(c) describes that the bearing vibration signals are obtained from an acceleration sensor fixed on the pedestal of the defective bearing. The driver motor rotary speed n = 1466 r/min, and the sampling frequency Fs = 12800 Hz. The bearing parameters shown in Table 5 are introduced into the Eq. (11), where the IRFF f_i = 132.2 Hz, and the ORFF f_o = 87.7 Hz can be obtained.

Figs. 21(a) and (b) present the experiment signal waveform and its ES, respectively. As seen, the ORFF f_o and its frequency doubling $2f_o$ - $5f_o$ are extracted effectively. The IRFF

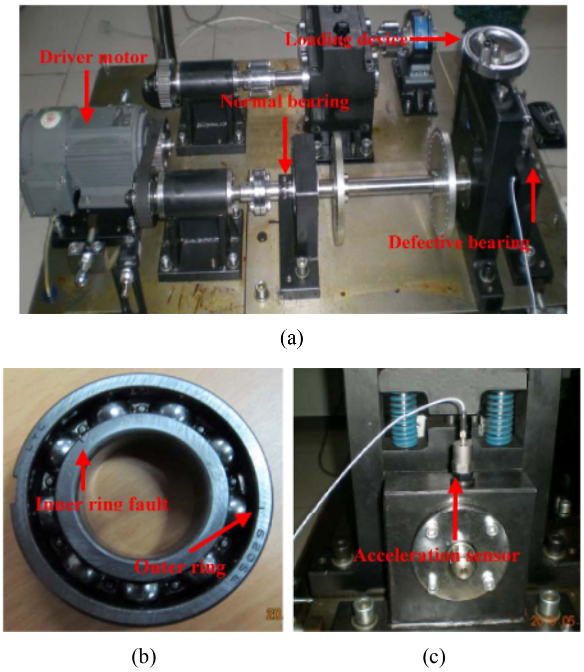

Fig. 20. (a) QPZZ test platform; (b) bearing with inner and outer ring fault; (c) acceleration sensor location.

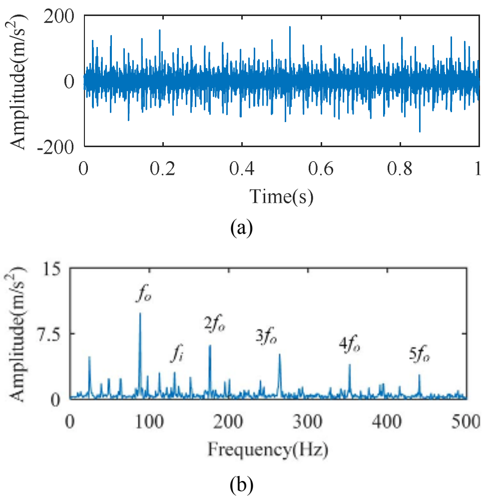

Fig. 21. (a) Experimental signal waveform; (b) ES of (a).

f_i can also be identified, but the amplitude of f_i is smaller than that of f_o and noise frequency, and thus is usually ignored.

The experiment fault signal is processed by EEMD-ICA method. Table 6 presents the correlation coefficient of each IMF component of initial signal. The IMF1–IMF6 components are used as the input parameter for ICA algorithm. Fig. 22 displays the diagnosis results. The ES of IC1 and IC2 shows that the ORFF f_o and its doubling frequency $2f_o$- $4f_o$ is more obvious, and the IRFF f_i is relatively weak. That is to say, the IRFF f_i is usually ignored.

The experiment fault signal is processed by WPT-SK method. Fig. 23(a) displays that the node (2, 2) has the maximum kurtosis value. Fig. 23(b) illustrates the ES of the frequency band signal corresponding to node (2, 2). As seen, the ORFF f_o and its doubling frequency $2f_o$ - $4f_o$ are identified productively whereas the IRFF f_i cannot be extracted.

The experiment fault signal is processed by E-Kurtogram method. Fig. 24(a) displays that the node (3, 3) has the maximum kurtosis value. Fig. 24(b) illustrates the ES of the frequency band signal corresponding to node (3, 3). As seen, the ORFF f_o and its doubling frequency $2f_o$ - $4f_o$ are identified productively whereas the IRFF f_i cannot be extracted.

The experiment fault signal is processed by the TEERgram method. Fig. 25(a) displays that the node (4, 4) has the maximum kurtosis value. Fig. 25(b) illustrates the ES of the frequency band signal corresponding to node (4, 4). As seen, the

Table 6. Correlation coefficient of IMFs.

IMF 1	IMF 2	IMF 3	IMF 4	IMF 5	IMF 6	IMF 7
1	0.7010	0.6510	0.3789	0.2884	0.1919	0.0883
IMF 8	IMF 9	IMF 10	IMF 11	IMF 12	IMF 13	IMF1 4
0.0547	0.0443	0.0336	0.0209	0.0153	0.0092	0.0014

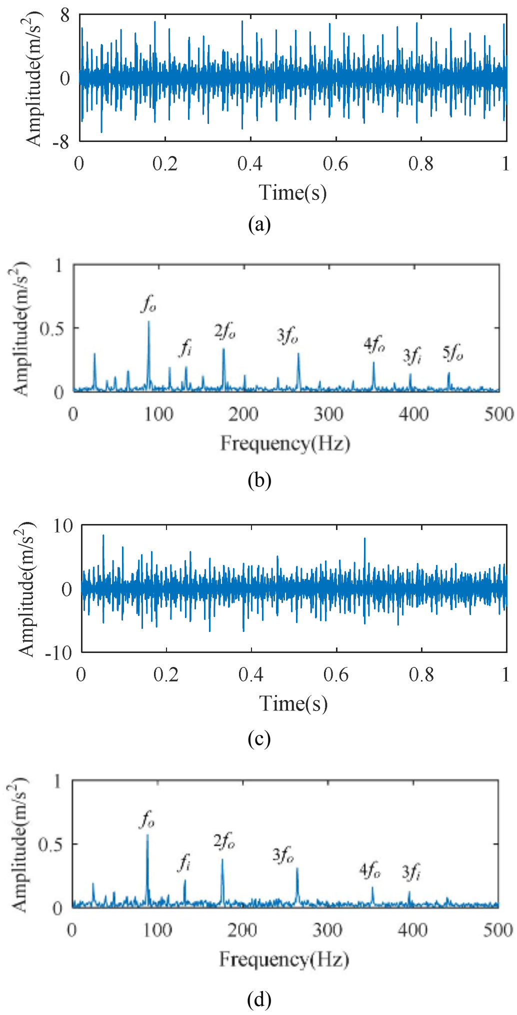

Fig. 22. Diagnosis results of the experiment signal 1: (a) IC 1 signal waveform; (b) ES of IC 1; (c) IC 2 signal waveform; (d) ES of IC 2.

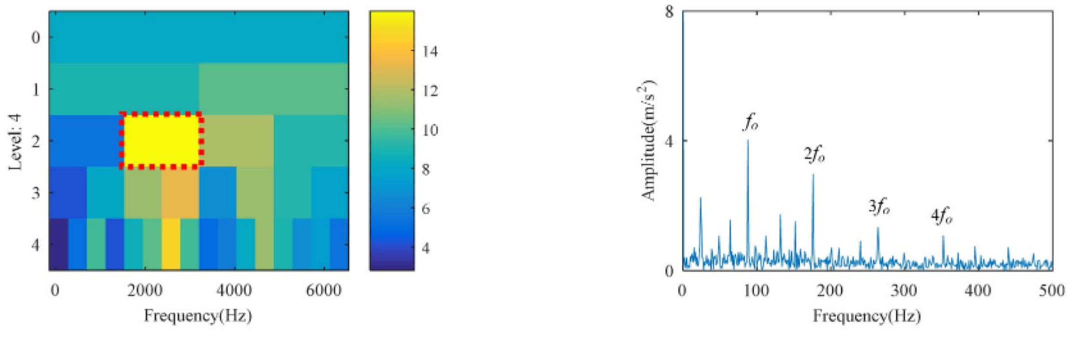

Fig. 23. Diagnosis results of the experiment signal 1: (a) Kurtgram; (b) ES of the signal corresponding to node (2, 2) in (a).

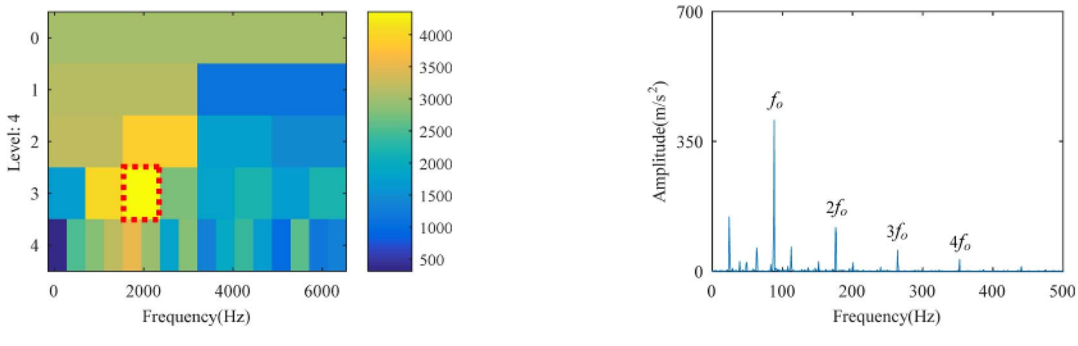

Fig. 24. Diagnosis results of the experiment signal 1: (a) E-kurtgram; (b) ES of the signal corresponding to node (3, 3) in (a).

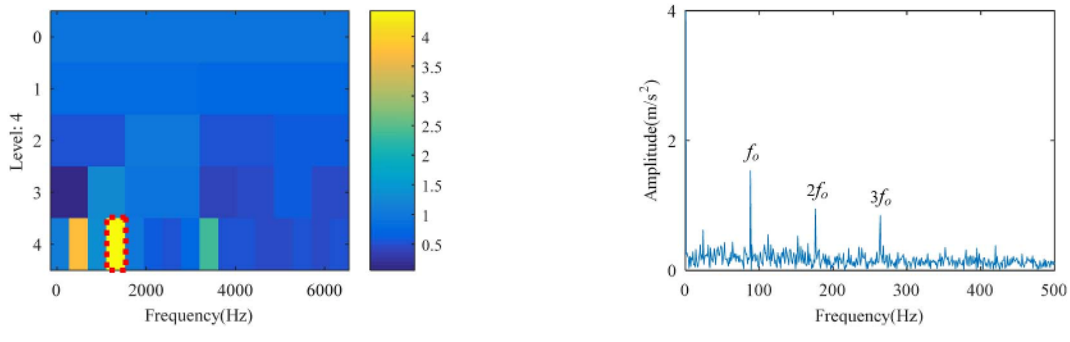

Fig. 25. Diagnosis results of the experiment signal 1: (a) TEERgram; (b) ES of the signal corresponding to node (4, 4) in (a).

ORFF f_o and its doubling frequency $2f_o$ - $3f_o$ are identified productively whereas the IRFF f_i cannot be extracted.

The experiment fault signal is processed by FERgram method. Fig. 26(a) displays the FERgram of outer ring fault. As shown, the maximum FER value is marked by the red rectangle and is at node (3, 2). That is to say, the frequency band signal corresponding to node (3, 2) contained the most outer ring fault information and its ES is presented in Fig. 26(b). As seen, the ORFF f_o and its frequency doubling $2f_o$ - $5f_o$ are extracted effectively. Fig. 26(c) displays the FERgram of the inner ring fault. As shown, the maximum FER value is marked by the red rectangle and is at node (3, 7). Thus the frequency band signal exacted from node (3, 7) is selected, as it contained the most inner ring fault information, and its ES is displayed in Fig. 26(d). As seen, the IRFF f_i and its frequency doubling $2f_i$ - $3f_i$ are identified productively.

In this case, the FERgram method can efficiently separate the fault information and accurately determine that the rolling bearing is under compound fault composed by inner and outer ring defective, while the EEMD-ICA method, WPT-SK method, E-Kurtogram method and TEERgram method cannot realize such functionality.

3.4 Experiment signal 2 analysis

The experimental signal of the rolling bearing under rolling element fault and outer ring fault is obtained from references [6]. The driver motor rotating speed n = 1300 r/min, and the sampling frequency Fs = 100000 Hz. The REFF f_e = 102.3 Hz, and the ORFF f_o = 86.3 Hz.

Figs. 27(a) and (b) present the experiment signal waveform and its ES, respectively. As seen, the ORFF f_o and its frequency doubling $2f_o$ - $5f_o$ are extracted effectively. The REFF f_e can not be identified.

The experiment fault signal is processed by EEMD-ICA method. Table 7 presents the correlation coefficient of each IMF component of initial signal. The IMF1–IMF6 components are used as the input parameter for ICA algorithm. Fig. 28 displays the diagnosis results. The ES of IC1 shows that the ORFF f_o and its doubling frequency $2f_o$ - $5f_o$ are more obvious, and the REFF f_e is not identified. The diagnosis result is consistent with reference [6].

The experiment fault signal is processed by WPT-SK method. Fig. 29(a) displays that the node (4, 9) has the maximum kurtosis value. Fig. 29(b) illustrates the ES of the frequency band signal corresponding to node (4, 9). As seen, the ORFF f_o and its doubling frequency $2f_o$ - $5f_o$ are identified productively whereas the REFF f_e cannot be extracted.

The experiment fault signal is processed by E-Kurtogram method. Fig. 30(a) displays that the node (4, 10) has the maximum kurtosis value. Fig. 30(b) illustrates the ES of the frequency band signal corresponding to node (4, 10). As seen,

Table 7. Correlation coefficient of IMFs.

IMF 1	IMF 2	IMF 3	IMF 4	IMF 5	IMF 6	IMF 7
1	0.5834	0.5088	0.4505	0.3326	0.2125	0.0714
IMF 8	IMF 9	IMF 10	IMF 11	IMF 12	IMF 13	IMF1 4
0.0237	0.0175	0.0083	0.0069	0.0032	0.0009	0.0007

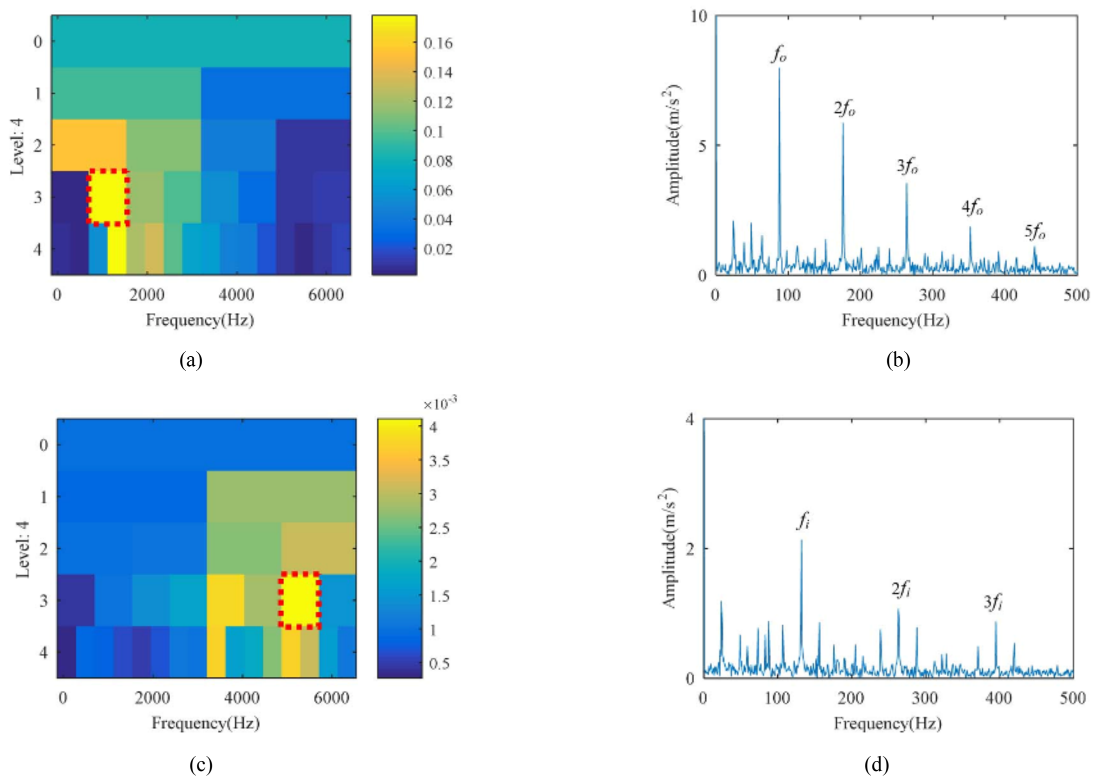

Fig. 26. Diagnosis results of the experiment signal using FERgram: (a) FERgram of outer ring fault; (b) ES of the signal corresponding to node (3, 2) in (a); (c) FERgram of inner ring fault; (d) ES of the signal corresponding to node (3, 7) in (c).

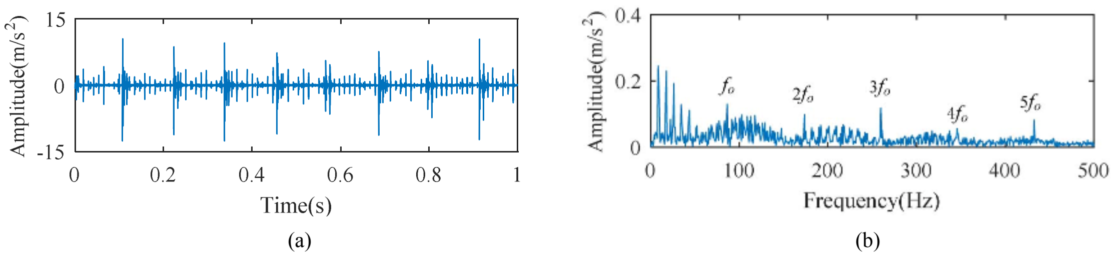

Fig. 27. (a) Experimental signal waveform; (b) ES of (a).

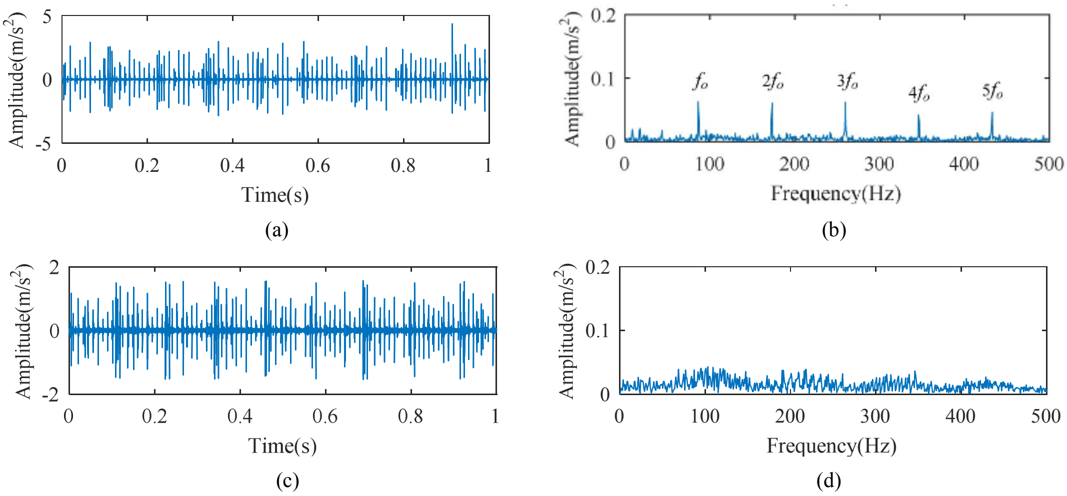

Fig. 28. Diagnosis results of the experiment signal 2: (a) IC 1 signal waveform; (b) ES of IC 1; (c) IC 2 signal waveform; (d) ES of IC 2.

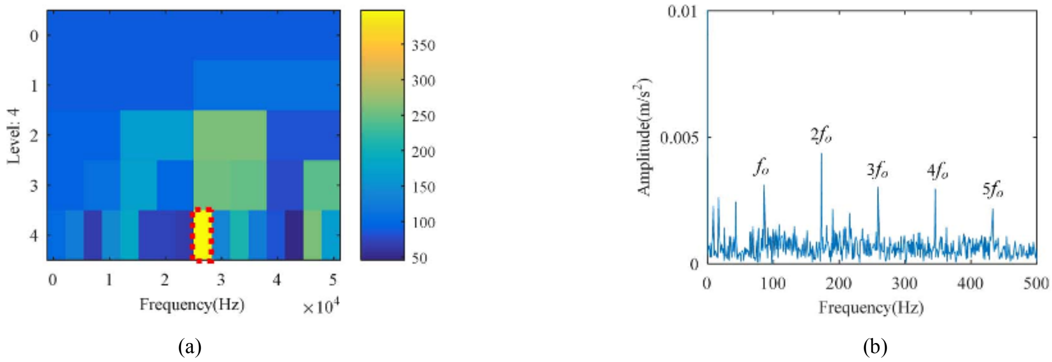

Fig. 29. Diagnosis results of the experiment signal 2: (a) Kurtgram; (b) ES of the signal corresponding to node (4, 9) in (a).

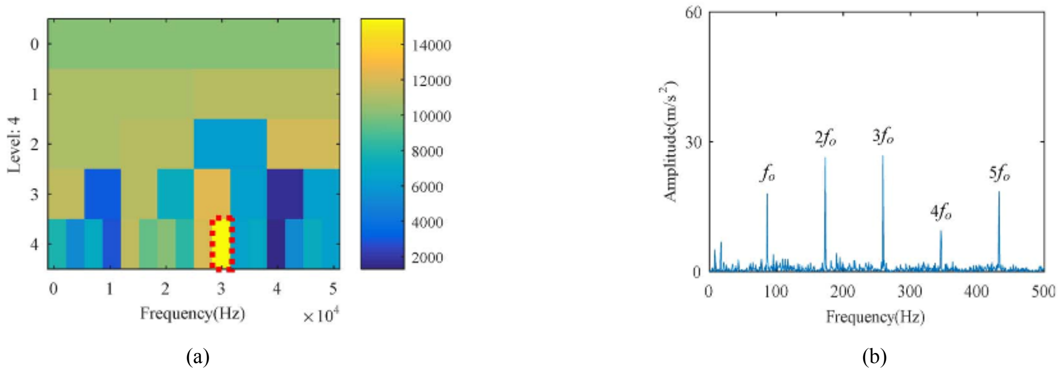

Fig. 30. Diagnosis results of the experiment signal 2: (a) E-kurtgram; (b) ES of the signal corresponding to node (4, 10) in (a).

the ORFF f_o and its doubling frequency $2f_o$ - $5f_o$ are identified productively whereas the REFF f_e cannot be extracted.

The experiment fault signal is processed by FERgram method. Fig. 31(a) displays the FERgram of outer ring fault. As shown, the maximum FER value is marked by the red rectangle and is at node (4, 10). That is to say, the frequency band signal corresponding to node (4, 10) contained the most outer ring fault information and its ES is presented in Fig. 31(b). As seen, the ORFF f_o and its frequency doubling $2f_o$ - $5f_o$ are extracted effectively. Fig. 31(c) displays the FERgram of the rolling element fault. As shown, the maximum FER value is marked by the red rectangle and is at node (4, 2). Thus the frequency band signal exacted from node (4, 2) is selected, as it contained the most rolling element fault information, and its ES is displayed in Fig. 31(d). As seen, although the IRFF f_e can be identified, the noise frequency interference is huge. The reason for this phenomenon may be that the rolling element fault is very weak, and thus the fault feature frequency is not very obvious.

TEERgram method needs data of the rolling bear under

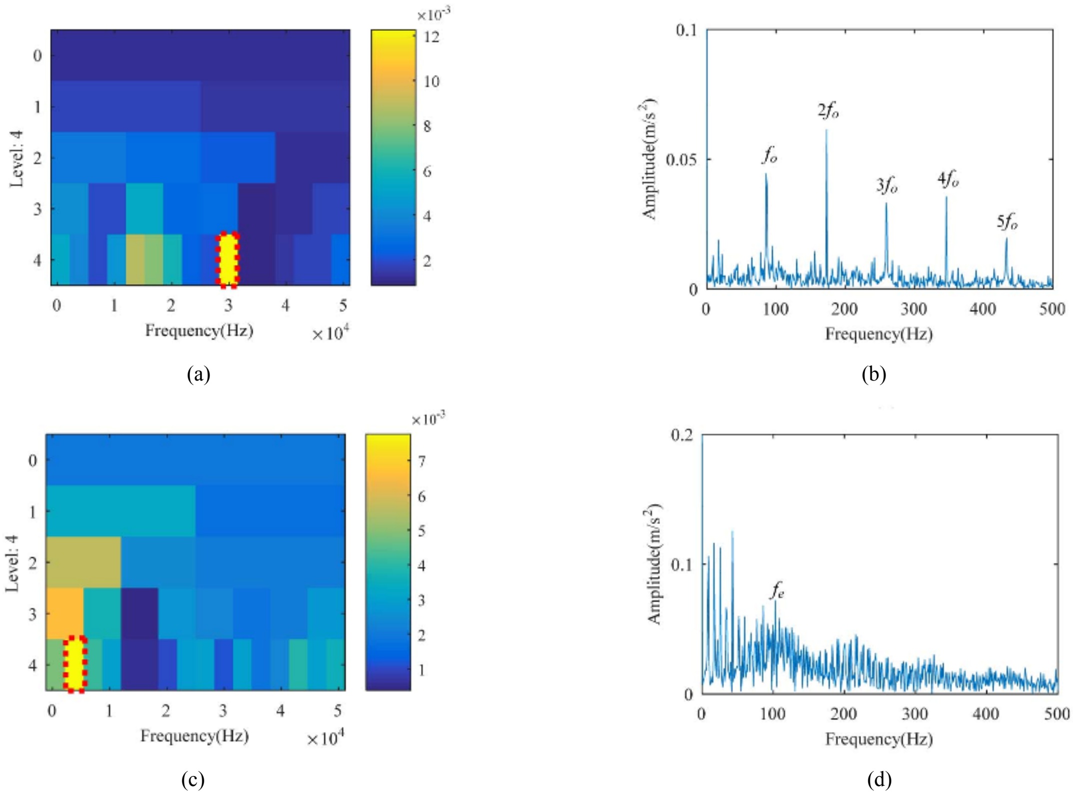

Fig. 31. Diagnosis results of the experiment signal 2: (a) FERgram of outer ring fault; (b) ES of the signal corresponding to node (4, 10) in (a); (c) FERgram of rolling element fault; (d) ES of the signal corresponding to node (4, 2) in (c).

both normal condition and fault condition. However, Ref. [6] didn't provide the data of the rolling bearing under normal condition, thus the TEERgram method is not used in this section as comparison.

In this case, the FERgram method can separate the fault information and accurately determine that the rolling bearing is under compound fault composed by outer ring and rolling element defective, while the EEMD-ICA method, WPT-SK method and E-Kurtogram method cannot realize such functionality.

4. Conclusions

Aiming to efficiently extract fault feature frequency and accurately diagnose the fault type of the rolling bearing, the present paper put forward a diagnosis method named FERgram. Comparing with the existing methods, the FERgram method has three improvements. (1) FER is applied replacing the traditional evaluation index, i.e. kurtosis index. (2) The FER value is calculated through Teager energy spectrum rather than envelope spectrum. (3) MODWOT rather than WPT is used to decompose signal. The feasibility and superiority of the FERgram method is demonstrated by four signals and four comparison method. The diagnosis results suggest that the FERgram method can effectively separate fault feature information and accurately determine the fault type of the rolling bearing.

Acknowledgments

This work was supported by the National Natural Science Foundation of China (No. 51777075).

References

[1] M. N. Yasir and B. Koh, Data decomposition techniques with multi-scale permutation entropy calculations for bearing fault diagnosis, *Sensors*, 18 (4) (2018) 1278.

[2] H. D. Yuan, J. Chen and G. M. Dong, An improved initialization method of D-KSVD algorithm for bearing fault diagnosis, *Journal of Mechanical Science & Technology*, 31 (11) (2017) 5161-5172.

[3] Y. J. Li, W. H. Zhang, Q. Xiong, D. B. Luo, G. M. Mei and T. Zhang, A rolling bearing fault diagnosis strategy based on improved multiscale permutation entropy and least squares SVM, *Journal of Mechanical Science & Technology*, 31 (6) (2017) 2711-2722.

[4] A. B. Ming, W. Zhang, Z. Y. Qin and F. L. Chu, Envelope calculation of the multi-component signal and its application to the deterministic component cancellation in bearing fault diagnosis, *Mechanical Systems & Signal Processing*, 50-51 (2015) 70-100.

[5] R. Peled, S. Braun and M. Zacksenhouse, A blind deconvolution separation of multiple sources, with application to bearing diagnostics, *Mechanical Systems & Signal Process-*

ing, 19 (6) (2005) 1181-1195.
[6] H. Q. Wang, R. T. Li, G. Tang, H. F. Yuan, Q. L. Zhao and X. Cao, A compound fault diagnosis for rolling bearings method based on blind source separation and ensemble empirical mode decomposition, *PLoS ONE*, 9 (10) (2014) e109166.
[7] L. L. Cui, C. G. Wu, C. Q. Ma and H. Q. Wang, Diagnosis of roller bearings compound fault using underdetermined blind source separation algorithm based on null-space pursuit, *Shock and Vibration*, 2015 (2015) 1-8.
[8] A. B. Ming, F. L. Chu and W. Zhang, Compound fault features separation of rolling element bearing based on the wavelet decomposition and spectrum auto-correlation, *Journal of Mechanical Engineering*, 49 (3) (2013) 80-87.
[9] H. Li, H. Q. Zheng and L. W. Tang, Bearing multi-fault diagnosis based on improved morphological component analysis, *Journal of Vibration & Shock*, 31 (12) (2012) 135-140.
[10] J. Antoni, The spectral kurtosis: A useful tool for characterising non-stationary signals, *Mechanical Systems & Signal Processing*, 20 (2) (2006) 282-307.
[11] J. Antoni and R. B. Randall, The spectral kurtosis: application to the vibratory surveillance and diagnostics of rotating machines, *Mechanical Systems & Signal Processing*, 20 (2) (2006) 308-331.
[12] J. Antoni, Fast computation of the kurtogram for the detection of transient faults, *Mechanical Systems & Signal Processing*, 21 (1) (2007) 108-124.
[13] Y. G. Lei, J. Lin, Z. J. He and Y. Y. Zi, Application of an improved kurtogram method for fault diagnosis of rolling element bearings, *Mechanical Systems & Signal Processing*, 25 (5) (2011) 1738-1749.
[14] D. Wang, P. W. Tse and K. L. Tsui, An enhanced Kurtogram method for fault diagnosis of rolling element bearings, *Mechanical Systems & Signal Processing*, 35 (1-2) (2013) 176-199.
[15] P. W. Tse and D. Wang, The design of a new sparsogram for fast bearing fault diagnosis: Part 1 of the two related manuscripts that have a joint title as "Two automatic vibration-based fault diagnostic methods using the novel sparsity measurement—Parts 1 and 2", *Mechanical Systems & Signal Processing*, 40 (2) (2013) 499-519.
[16] P. W. Tse and D. Wang, The automatic selection of an optimal wavelet filter and its enhancement by the new sparsogram for bearing fault detection: Part 2 of the two related manuscripts that have a joint title as "Two automatic vibration-based fault diagnostic methods using the novel sparsity measurement—Parts 1 and 2", *Mechanical Systems & Signal Processing*, 40 (2) (2013) 520-544.
[17] T. Barszcz and A. JabŁoński, A novel method for the optimal band selection for vibration signal demodulation and comparison with the Kurtogram, *Mechanical Systems & Signal Processing*, 25 (1) (2011) 431-451.
[18] B. Q. Chen, Z. S. Zhang, Y. Y. Zi, Z. J. He and C. Sun, Detecting of transient vibration signatures using an improved fast spatial–spectral ensemble kurtosis kurtogram and its applications to mechanical signature analysis of short duration data from rotating machinery, *Mechanical Systems & Signal Processing*, 40 (1) (2013) 1-37.
[19] G. Yu, C. N. Li and J. F. Zhang, A new statistical modeling and detection method for rolling element bearing faults based on alpha–stable distribution, *Mechanical Systems & Signal Processing*, 41 (1-2) (2013) 155-175.
[20] P. Borghesani, P. Pennacchi and S. Chatterton, The relationship between kurtosis- and envelope-based indexes for the diagnostic of rolling element bearings, *Mechanical Systems & Signal Processing*, 43 (1-2) (2014) 25-43.
[21] J. Antoni, The infogram: Entropic evidence of the signature of repetitive transients, *Mechanical Systems & Signal Processing*, 74 (2016) 73-94.
[22] S. T. Wan, X. Zhang and L. J. Dou, Shannon entropy of binary wavelet packet subbands and its application in bearing fault extraction, *Entropy*, 20 (4) (2018) 260.
[23] S. T. Wan and X. Zhang, Teager energy entropy ratio of wavelet packet transform and its application in bearing fault diagnosis, *Entropy*, 20 (5) (2018) 388.
[24] A. T. Walden, *Wavelet analysis of discrete time series*, European Congress of Mathematics (2001) 627-641.
[25] L. Shen, X. J. Zhou, W. B. Zhang and Z. G. Zhang, Application of morphological demodulation in gear fault feature extraction, *Journal of Zhejiang University*, 44 (8) (2010) 1514-1518.
[26] T. J. Wang, Z. P. Feng, R. J. Hao and F. L Chu, Fault diagnosis of rolling element bearings based on teager energy operator, *Journal of Vibration & Shock*, 31 (2) (2012) 1-5, 85.
[27] R. B. Randall and J. Antoni, Rolling element bearing diagnostics—A tutorial, *Mechanical Systems & Signal Processing*, 25 (2) (2011) 485-520.
[28] H. B. Hong and M. Liang, Separation of fault features from a single-channel mechanical signal mixture using wavelet decomposition, *Mechanical Systems & Signal Processing*, 21 (5) (2007) 2025-2040.
[29] Bearing data center, Case Western Reserve University, *http://csegroups.case.edu/bearingdatacenter/home*.

Shuting Wan is a Professor at the School of Mechanical Engineering in North China Electric Power University. He obtained his Ph.D. from the North China Electric Power University, China, in 2006. His research interests include condition monitoring and fault diagnosis of power equipment.

Bo Peng is a Ph.D. student at the School of Mechanical Engineering in North China Electric Power University. His research interest is condition monitoring and fault diagnosis of power equipment.